J Solid State Electrochem (2009) 13:551–563
DOI 10.1007/s10008-008-0751-8

ORIGINAL PAPER

Theoretical and experimental evaluation of screen-printed tubular carbon ink disposable sensor well electrodes by dc and Fourier transformed ac voltammetry

Anastassija Konash · Alexander R. Harris · Jie Zhang · Darrell Elton · Mark Hyland · Gareth Kennedy · Alan M. Bond

Received: 14 October 2008 / Revised: 19 November 2008 / Accepted: 19 November 2008 / Published online: 23 December 2008

Abstract Mass-produced, screen-printed, carbon-ink-based microtubular band (well) electrodes, suitable for routine sensing applications, have been fabricated and evaluated with respect to their theoretical and analytical performance. Microscopic examination of the electrode surface reveals they are inherently rough and could easily suffer from high and variable resistance, capacitance and area, unless care is taken to minimise these problems. Simulation models have been applied to analyse cyclic voltammetric responses obtained at the well electrodes. Results of these theoretical calculations further demonstrate the care needed with electrode design and resistance in carbon ink electrodes. Substantial differences in voltammetry when wells are produced by mechanically punching or laser drilling are considered. The application of multi- and single-frequency Fourier Transform ac voltammetry, previously applied to planar carbon ink disc electrodes for quality control purposes, is now demonstrated with respect to the microtubular band electrode geometry. Theoretical and practical limitations are discussed, as is the analytical application to the reversible $\left[Ru(NH_3)_6\right]^{3+}+e^- \rightleftharpoons \left[Ru(NH_3)_6\right]^{2+}$ redox couple in the presence of oxygen in aqueous solution.

Keywords Screen-printed tubular band electrodes · Well electrodes · Fourier Transform ac voltammetry · Electrode performance

Dedicated to Keith on his 80th birthday, a good friend and colleague.

A. Konash · A. R. Harris · J. Zhang · G. Kennedy · A. M. Bond (✉)
School of Chemistry and ARC Centre for Green Chemistry,
Monash University,
Clayton, Victoria 3800, Australia
e-mail: alan.bond@sci.monash.edu.au

A. R. Harris · M. Hyland
Oxford Biosensors Ltd, Oxford Industrial Park,
Mead Road,
Yarnton OX5 1QU, Oxfordshire, UK

J. Zhang
Institute of Bioengineering and Nanotechnology,
31 Biopolis Way,
The Nanos #04-01, Singapore

D. Elton
Department of Electronic Engineering, Latrobe University,
Bundoora, Victoria 3086, Australia

Introduction

Screen-printed electrodes (SPEs) have become common in the field of low cost electrochemical sensing [1–5]. The almost infinite number of SPE designs available include: (a) tubular band electrodes designed specifically for field use in flowing solutions [6]; (b) microdisc electrodes having convergent (or nonlinear) diffusion, which allow a favourable Faradaic to capacitive current ratios and low Ohmic (IR_u) drop effects to be achieved [7] and (c) recessed electrodes where a working electrode of designated geometry (disc, ring, band) is incorporated into the bottom or side of a well [8]. In the present study, a carbon-ink-based microtubular band electrode inside a well, and hence referred to as a well electrode, has been developed via screen printing, with the well produced by mechanical punching or laser ablation techniques [9–13]. The purpose of the well is to provide a known volume for enzymatic and other reactions of interest.

The microtubular band electrode geometry which is relevant to the well electrode configuration initially received considerable attention due to the possibility of

combining attractive features of microelectrode-like behaviour (minimal IR_u drop and background current) with macroelectrode area (high analytical sensitivity). Theoretical treatments of this geometry are available with respect to the techniques of chronoamperometry and cyclic voltammetry [14–18]. Simulations available for a reversible process have demonstrated that when the length of the tubular microelectrode is much larger than its width (thickness of the carbon ink layer for a SPE), tubular band electrodes behave similarly to microband electrodes [17], which in turn can be approximated by an equivalent hemicylidrical diffusion model [6, 18, 19] in which the length of the equivalent hemicylinder is equal to the radius of the tubular band tube multiplied by 2π and the radius of the hemicylinder is equal to the width of the microband divided by 4 at low scan rates and by π at high scan rates [18].

In this study, a range of designs that produce microband electrodes within a well have been considered and their analytical performance evaluated. A simulation based on the tubular band concept has been developed and used in conjunction with models available in commercially available simulation packages to predict the nature of the voltammetric behaviour obtained with the SPE well design and to understand problems encountered with IR_u drop. Background current, presence of oxygen and activation of the carbon surface caused by laser ablation also are evaluated. Simulated voltammograms obtained from the equivalent hemicylinder approach and the model developed in this paper are compared with experimental data obtained with the $\left[Ru(NH_3)_6\right]^{3+}+e^- \rightleftharpoons \left[Ru(NH_3)_6\right]^{2+}$ process. Finally, data obtained by multi-frequency and single-frequency Fourier transform (FT) ac voltammetry [20] are utilised to assess the reproducibility of well electrode manufacture and to further examine issues related to uncompensated resistance and capacitance. Limits of detection obtained by dc and ac voltammetric techniques are compared, and the advantage of discrimination against the oxygen reduction process available with the ac method is assessed.

Experimental

Electrode fabrication

The electrode fabrication process (Fig. 1) is based on procedures reported in [9, 10, 20, 21]. A plastic substrate provides the platform, onto which the various inks [silver ink (Coates 26-8204), carbon ink (DuPont E104195-80A), dielectric ink (Ercon E6165-116), Ag/AgCl layer (Ercon

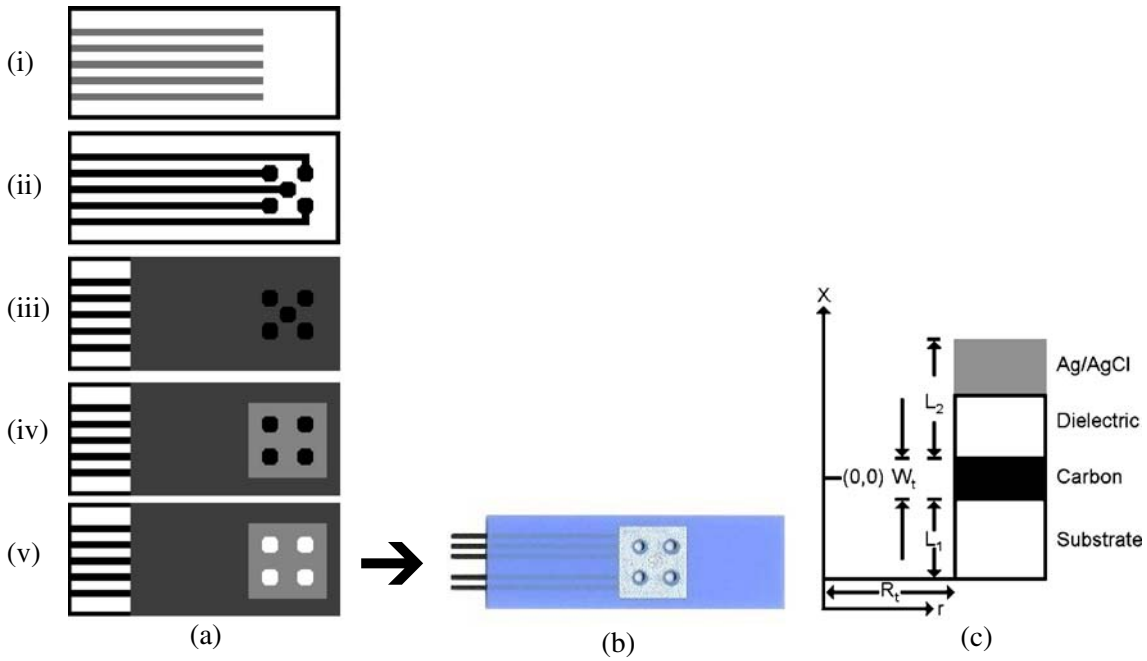

Fig. 1 **a** Side view illustrating the method for manufacturing well SPEs. From *top to bottom*, (*i*) plastic substrate used as a support; (*ii*) silver tracks printed onto the substrate, followed by carbon tracks and pads; (*iii*) a dielectric film masking the electrode legs printed on top; (*iv*) addition of a Ag/AgCl reference; (*v*) holes punched or drilled through the carbon pads. **b** Image of a well electrode strip. **c** A vertical section cut though the centre of the well containing the coordinate system used for the well electrode simulation. All parameters are given in centimetre and are defined as follows: x is the distance from the centre of the carbon ink layer and it can be positive or negative; r is the distance from the centre of the well to the wall of the well and can have a value from 0 to R_t; W_t is the width of the electrode; L_1 is the depth of the well from the carbon ink layer to the bottom of the well; L_2 is the depth of the well from the top of the well to the carbon ink layer

E0430-128)] are printed. The procedure is described in detail in [20] and is summarised in Fig. 1. To create the well electrodes, holes were mechanically punched (Preco press) or laser drilled (OpTek Systems) through the four carbon pads to create four well electrodes on one strip. Normally, a plastic backing sheet (mechanically punched electrodes) or hydrophobic membrane (laser-drilled electrodes) was glued to the rear of the substrate to form the base of the well. A schematic representation of a vertical section, cut through the centre of a mechanically punched well electrode, is shown in Fig. 1c. A scanning electron microscopy (SEM) microphotograph of a section of a laser-drilled well electrode is shown on Fig. 2. The SEM image was obtained using a JEOL JSM-840A microscope. The sample was prepared by freezing the chip with the electrodes in liquid nitrogen followed by cutting the well perpendicular to the screen printing plane. Microscopic examination using an optical microscope revealed that the diameter of the wells was reproducibly 0.10 cm.

Large numbers of well electrodes were produced simultaneously on the plastic substrate in each screen printing run. Individual strips were cut out from the production sheet and inserted into a standard electrical connector (JST) via the electrode legs to give a configuration in which each of the four carbon ink electrodes and the Ag/AgCl reference electrode could be controlled electrochemically. The SPE arrays were dipped directly into the test solution. In the case of a three-electrode potentiostated experiment, one well electrode was used as the working electrode, the Ag/AgCl layer was the reference electrode and platinum gauze was placed in solution to become the auxiliary electrode. In the two-electrode experimental setup, one carbon ink working and the Ag/AgCl reference electrodes were used. In this case, both the counter and reference electrode inputs of the potentiostat were connected to the reference electrode. The two-electrode configuration has the advantages of simplicity and cost with respect to instrumentation. This mode also requires one less electrode and allows for more flexibility in strip design and minimises requirements for registration of multiple print layers. Clearly, the advantages of the three-electrode configuration include minimisation of IR_u drop and provision of a more stable reference potential because of avoidance of current flowing through the reference electrode.

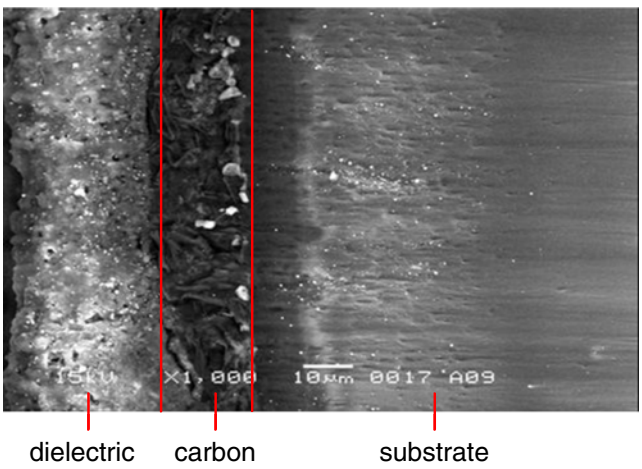

Fig. 2 SEM image of a batch **2** screen-printed electrode

Chemicals

Reagent grade KCl, $NaH_2PO_4{\cdot}H_2O$, Na_2HPO_4 (BDH), $[Ru(NH_3)_6]Cl_3$ (Strem), $K_3[Fe(CN)_6]$, and NaOH (Sigma) were used as received from the manufacturer. Phosphate buffer solutions (0.1 or 0.05 M) were prepared from $NaH_2PO_4{\cdot}H_2O$ and Na_2HPO_4. In order to study the effect of the pH on the $[Fe(CN)_6]^{3-/4-}$ voltammetry, 50 mM phosphate buffer was prepared in a 150 mM solution of KCl. The buffer was adjusted to pH 3.5, 6.0 or 8.2 using HCl or NaOH. In limit of detection studies, $[Ru(NH_3)_6]^{3+}$ (0.1 μM–5 mM) solutions were prepared daily in 0.05 M phosphate buffer (pH 6.7) containing 0.45 M KCl. All solutions were made up with water (resistivity of 18.2 MΩ cm) obtained from a Milli-Q purification system (Millipore).

Instrumentation and procedures

dc voltammetric experiments were performed with either Autolab PGSTAT100 (ECO-Chemie) or BAS 100B electrochemical workstations. FT ac voltammetric measurements were undertaken with custom-built instrumentation [22]. Multi-sine wave applications introduced to assess resistance (R_s) and capacitance (C_s) of the electrochemical cell used waveforms and procedures detailed elsewhere [20]. Screen-printed electrodes were manufactured as detailed above. All voltammetric experiments were performed at 20±2°C, and without removal of oxygen from the solution, unless otherwise stated. In the dc voltammetry, the potential was typically scanned from 200 to −500 mV vs Ag/AgCl at a designated scan rate. In the ac case, one or more sine waves of frequency (f) and amplitude (ΔE) were superimposed onto the dc ramp [22] which was swept at a designated rate.

Modelling of the Faradaic, background and resistance components of a well electrode

Initially, experimental data obtained with the well electrode were compared to predictions based on simulations available from commercial software packages (DigiSim and DigiElch) that use hemicylidrical and band microelectrode geometries where the only geometric parameters of interest are the radius (R), length (L) and width (W) of the electrode.

As was described in "Introduction", for a reversible and fast electron transfer process, the current obtained on the tubular band electrode can be modelled using a microband electrode approximation [6]. Thus, the dimensions of the tubular band can be translated to the microband as follows: the width of the tubular band (W_t) is equivalent to the width of the microband (W_{mb}), and the length of the microband (L_{mb}) is equivalent to the circumference of the tubular band ($2\pi R_t$) [6]. In the case when $8W_t^{-1}(DRT/Fv)^{1/2}$ (where D is diffusion coefficient, v is the scan rate, R is the gas constant, F is Faraday's constant, T is the temperature) is less than 10, the microband behaviour can be described using a hemicylindrical geometry with equivalent hemicylinder dimensions as follows: the radius $R_{hc}=W_{mb}/\pi=W_t/\pi$ and the length $L_{hc}=L_{mb}=2\pi R_t$ [18].

The hemicylindrical geometry was used to model the ac and dc components of the FT ac voltammetry. Simulations for the single charge transfer mechanism were carried out using a new software package developed in-house called MECSim (Monash Electrochemistry Simulator). This package is written in Fortran 77 and is based on the matrix formulation outlined in reference [23]. It has the advantage over present simulation packages, such as DigiSim, that ac signals and nonlinear capacitors can be added with ease. Details of this simulation package will be presented in an upcoming paper and copies of the software are available on request.

In order to introduce features associated with the well, not present in the model described above, a more complete simulation was developed, relevant to the parameters summarised in Fig. 1c that introduce parameters such as L_1, L_2 and R_t that describe the well dimensions.

The electrode reaction employed to model the Faradaic component of the screen-printed working electrode in the well electrode configuration (Fig. 1c) is based on the one-electron $\left(\left[Ru(NH_3)_6\right]^{3+}+e^- \rightleftharpoons \left[Ru(NH_3)_6\right]^{2+}\right)$ transfer process described by Eq. 1:

$$Ox + e^- \underset{k_b}{\overset{k_f}{\rightleftharpoons}} Red \tag{1}$$

In this reaction, Ox and Red are the oxidised ($[Ru(NH_3)_6]^{3+}$) and reduced ($[Ru(NH_3)_6]^{2+}$) forms, respectively, and k_f and k_b are the heterogeneous forward and reverse rate constants for the electron transfer step. The electron transfer process is assumed to be described (Eq. 2) by the Butler–Volmer relationship [24]:

$$k_f = k^{0'}\exp\left[\frac{-\alpha F}{RT}\left(E-E^{0'}\right)\right] \text{ and}$$
$$k_b = k^{0'}\exp\left[\frac{(1-\alpha)F}{RT}\left(E-E^{0'}\right)\right] \tag{2}$$

where E, $E^{0'}$, $k^{0'}$ and α are the potential of the working electrode versus the reference electrode, the formal reversible potential, the formal electron charge transfer rate constant at potential $E^{0'}$ and the charge transfer coefficient, respectively, whilst F, R and T have their usual meanings.

The mass transport to the working electrode in the well is considered to occur solely by diffusion [17]. If the screen-printed carbon working electrode is regarded as having tubular band geometry, the diffusion process may be described by Fick's Law in the form [17]:

$$\frac{\partial c}{\partial t} = D\left(\frac{\partial^2 c}{\partial r^2}+\frac{1}{r}\frac{\partial c}{\partial r}+\frac{\partial^2 c}{\partial x^2}\right). \tag{3}$$

The coordinate system used for the well electrode of interest in this work is shown in Fig. 1c. Equation 3 can be solved using the following initial and boundary conditions:

$t=0$, all x and all r:

$$c_{ox} = c_{ox}^*, c_{red} = 0 \tag{4}$$

$t>0$, zero flux condition applied to all non-conductive substrates and the central axis of the tube, including (a) $x=0$, all r; (b) $x=-W_t/2-L_1$, r from 0 to R_t; (c) x from $-W_t/2-L_1$ to $-W_t/2$, $r=R_t$; (d) x from $W_t/2$ to $W_t/2+L_2$, $r=R_t$ and (e) $x=W_t/2+L_2$, $r\geq R_t$.

$t>0$, at the electrode surface:

$$-D_{ox}\frac{\partial c_{ox}}{\partial r} = D_{red}\frac{\partial c_{red}}{\partial r} = k_f c_{ox} - k_b c_{red} \tag{5}$$

$t>0$, $x=\infty$ and all r:

$$c_{ox} = c_{ox}^*, c_{red} = 0 \tag{6}$$

where c_{ox}^* is the bulk concentration and D_{ox} the diffusion coefficient of Ox. Current, I, can be calculated [17] according to Eq. 7 once the concentration gradient is known at potential E.

$$\frac{I}{FD_{ox}} = 2\pi R_t\int_{-W_t/2}^{W_t/2}\left(\frac{\delta c_{ox}}{\delta r}\right)_{r=R_t}\mathrm{d}x. \tag{7}$$

Effectively, the model is based on a well electrode configuration that has been cut in half (Fig. 1c). This strategy enabled the cell geometry factors of electrode width (W_t), radius of the well (R_t), depth of the well between carbon layer and plastic substrate (L_1), depth of the well from the top to the carbon ink layer (L_2), as well as the standard terms of $k^{0'}$, α, D, concentration (c) and the uncompensated resistance (R_u) to be conveniently parameterised.

Simulations of voltammograms for the well electrode were based on solving Eqs. 2, 3 and 7 and were achieved with the alternating direction implicit finite difference method [25]. The current density along the edge of the well electrode is significantly higher in the region where radial diffusion makes a significant contribution to the mass

transport [26]. In order to accurately calculate the Faradaic current under conditions of a non-uniform current density, an expanding space grid [27] was used in order to achieve highly accurate numerical simulations without losing efficiency. This approach has been previously adopted in the simulation of the Faradaic response at microdisc [25, 28] and microring [29] electrodes. It was assumed that no convection or migration was contributing to the current generated. The reference electrode was assumed to be located infinitely far from the working electrode and possess infinitely large area. The effect of uncompensated resistance was included in the simulation using a widely employed procedure [30]. The code needed for the computation was implemented in Fortran 77 and is available on request to the authors.

Results and discussion

Characteristics of screen-printed electrodes

dc cyclic voltammetry

Initially, well electrodes prepared by mechanical punching (batch **1′**) had extremely thin carbon layers and no silver layer was present underneath the carbon layer. The performance was assessed using dc cyclic voltammetry of 0.5 mM $[Ru(NH_3)_6]^{3+}$ in 0.5 M KCl at a scan rate of 100 mVs^{-1}. Electrodes based on these features produced highly variable performance. Typically, these electrodes produced cyclic voltammograms with very small peak currents (always ≤10 nA and typically 6 nA) and with an oxidation–reduction peak-to-peak splitting (ΔE_p) of about 200 mV (scan rate=100 mV s^{-1}; Fig. 3a), implying the presence of very high resistance. Some electrodes tested from this initial design actually exhibited close to linear dc current versus potential plots (Fig. 3b) which is usually associated with a pure resistor. Inspection of these electrodes revealed that mechanical punching of the well electrode in the case of carbon layers with a thickness approaching that of the carbon particle size could lead to blocking of the carbon electrode surface. Furthermore, some electrodes exhibited current spikes and/or a limiting current for reduction of $[Ru(NH_3)_6]^{3+}$ followed by a large current associated with reduction of oxygen followed by a smaller than expected oxidation current when the potential direction was switched. All these behaviours indicated highly variable and large resistances, stripping of contaminant Ag from the reference electrode, breakdown/functionalisation of the ink, sometimes enhanced reduction of oxygen and generally unsatisfactory performance.

After addressing the problems identified above, a batch of more successful mechanically punched well electrodes (batch **1**) were prepared using the protocol given in Fig. 1.

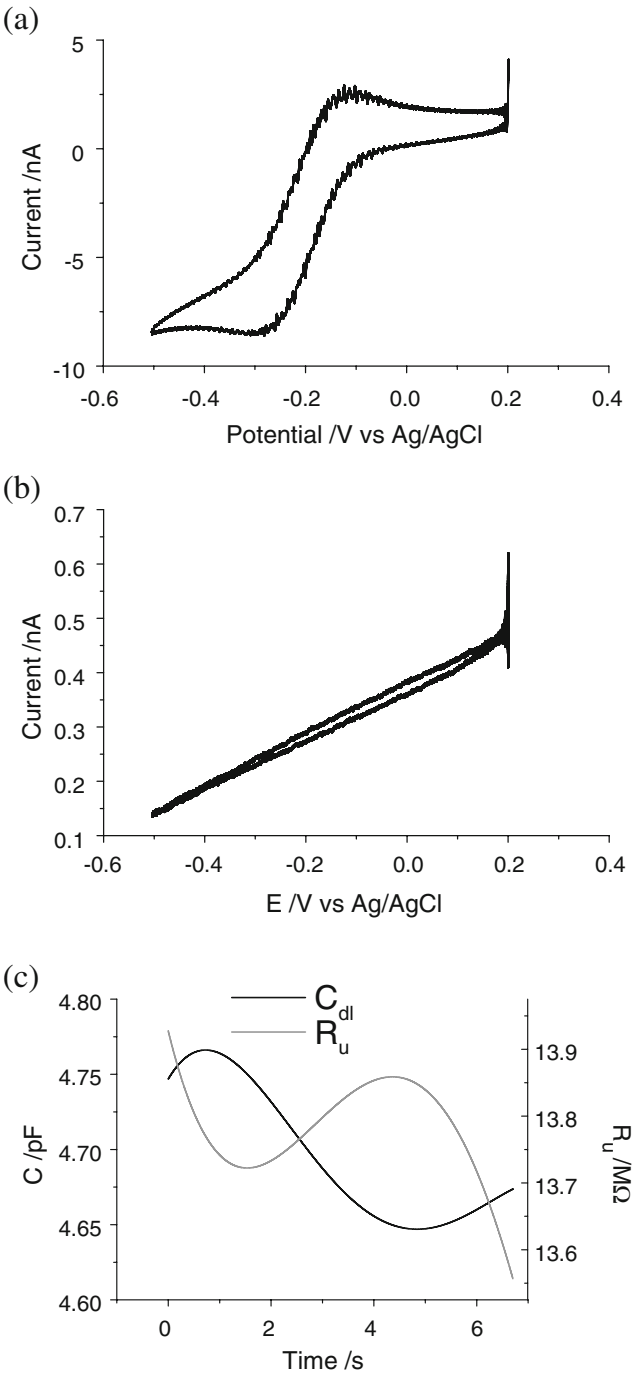

Fig. 3 **a**, **b** dc components of an FT ac voltammetric experiment (f= 35.17, 90.00, 230.07, 370.14 and 590.09 Hz, ΔE=30 mV, scan rate= 100 mV s^{-1}) for well (**a**) and poorly behaved mechanically punched batch **1′** electrodes (**b**). **c** R_s and C_s values of electrode in (negative potential direction scan) (**b**) for reduction of 0.5 mM $[Ru(NH_3)_6]^{3+}$ in 0.5 M KCl using a two-electrode configuration

In particular, a silver layer was printed underneath the carbon ink, and the carbon layer was now significantly thicker than the size of individual carbon particles present in the carbon ink (see below). In this case, the cyclic voltammograms obtained for reduction of $[Ru(NH_3)_6]^{3+}$

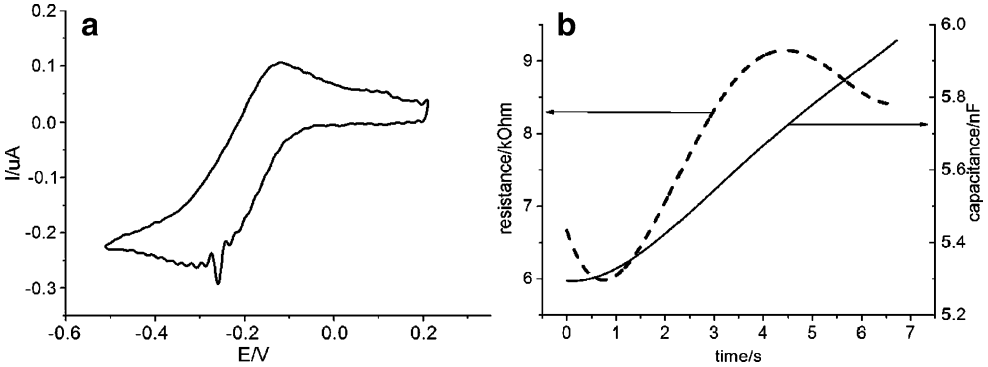

Fig. 4 **a** dc components of an FT ac voltammetric experiment (f= 35.17, 90.00, 230.07, 370.14 and 590.09 Hz, ΔE=30 mV, scan rate=100 mV s^{-1}) for a mechanically punched batch **1** electrode. **b** R_s and C_s values (negative potential direction scan) for reduction of 0.5 mM $[Ru(NH_3)_6]^{3+}$ in 0.5 M KCl using a three-electrode configuration

had similar shapes to some of the originally produced electrodes, but the dc peak current was now reproducibly of the order of 270 nA (Fig. 4a) rather than 6 nA obtained with the originally designed electrodes, indicating a much larger electroactive area had been achieved.

A second generation of SPEs (method **2**) was developed, again based on the protocol in Fig. 1. However, in this case, laser drilling rather than mechanical punching was used to produce the wells. The laser drilling provides highly reproducible electrode shapes and sizes and drastically decreases the damage to the electrode evident in the mechanical punching method where physical contact of the stamp with the inks can cause smearing or even breakage of the ink layer. The SEM microphotograph (Fig. 2) obtained with such electrodes demonstrates that the thickness of the carbon layer is not fully constant over the whole length of the electrode. Typically, variations of ±2 μm are present in different parts of the electrode. The average width can be varied between 10 and 20 μm, but the majority used in these studies had a width of 18±2 μm. Batch **2** electrodes produced current values close to those observed with batch **1** electrodes under conditions of cyclic voltammetry with the $[Ru(NH_3)_6]^{3+/2+}$ process when they had similar electrode widths (Fig. 5a). However, laser-drilled electrodes displayed the oxygen reduction process at less negative potentials (now almost overlapping the $[Ru(NH_3)_6]^{3+/2+}$ process) and a larger background capacitive current, consistent with a more active electrode surface [31–35].

Pulsed laser ablation of carbon paste and graphite electrodes has been reported [31–35] to produce preferential ablation of binder and contaminant material from the carbon surface, hence generating a cleaner electrode surface [32]. Ablation in the presence of oxygen also was reported to lead to functionalisation of the carbon surface, which drastically increased the electron transfer rate for the $[Fe(CN_6)]^{3-/4-}$ process and markedly enhanced the capacitance of the carbon surface [31, 33]. Consistent with these findings, the cyclic voltammetry of $[Fe(CN_6)]^{3-/4-}$ demonstrated a much higher apparent electron transfer rate for the $[Fe(CN_6)]^{3-/4-}$ process at laser-drilled SPEs relative to mechanically punched ones as evidenced by smaller values of the peak-to-peak separation in reduction and oxidation processes on laser drilled SPEs at all pH values examined (Fig. 6a, b). The work of Girault et al. [33, 34] and others may be consulted for more details on the relationship of heterogeneity, pH and related aspects of the $[Fe(CN_6)]^{3-/4-}$ process on carbon electrodes.

Determination of resistance and capacitance using Fourier transformed ac voltammetry

FT ac voltammetry can rapidly provide details on the background current, capacitance (C) and resistance (R) which are parameters that can be related to quality control of mass-produced SPE sensors [20, 22, 30]. The usefulness of the FT ac voltammetric method in assessment of electrode manufacture is clearly revealed in studies with

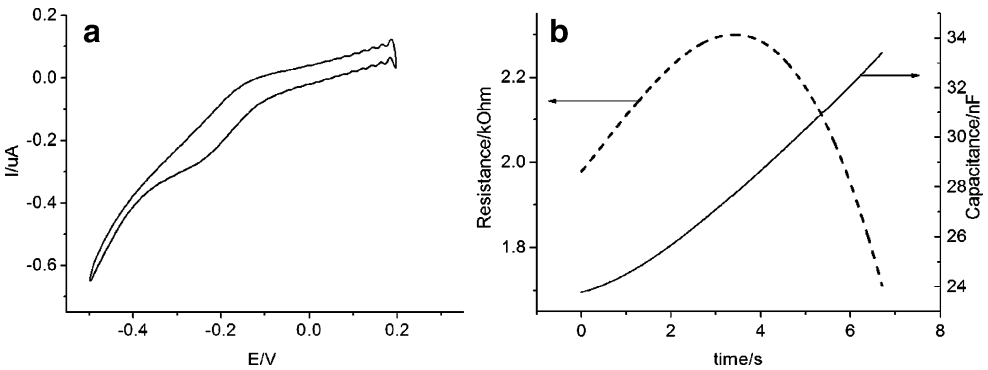

Fig. 5 **a** dc component of an FT ac voltammetric experiment (f= 37.10, 92.39, 229.92, 372.90 and 589.94 Hz, ΔE=30 mV, scan rate=100 mV s^{-1}) for a laser-drilled batch **2** electrode. **b** R_s (*dash*) and C_s (*solid*; negative potential direction scan) for the reduction of 0.5 mM $[Ru(NH_3)_6]^{3+}$ in 0.5 M KCl using a three-electrode configuration

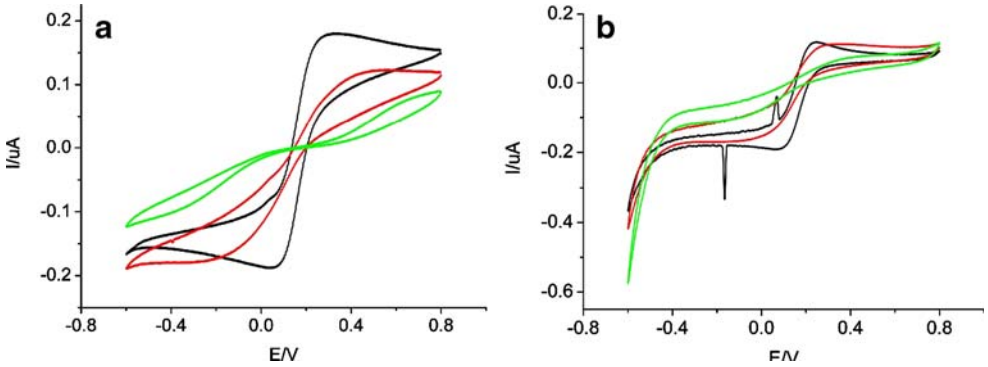

Fig. 6 dc voltammetry at a scan rate of 100 mV s^{-1} for reduction of 1 mM $[Fe(CN)_6]^{3-}$ batch **1** (**a**) and batch **2** (**b**) electrodes (pH=8.2 *green*; pH=6 *red*, pH=3.5 *black*)

well electrodes even when using the simplest possible model of a *RC* circuit based on a resistor (R_s) and capacitor (C_s) in series [20].

Analysis of FT ac voltammograms using the R_sC_s model with 0.5 M KCl electrolyte with and without 0.5 mM $[Ru(NH_3)_6]^{3+}$ (Fig. 3c and Table 1) confirm that a significant cause of the non-reproducible voltammetry of mechanically punched batch **1′** well electrodes is the high and variable R_s and very small and variable C_s values (small electrode areas from very thin tubular bands). Much more reproducible R_s and C_s characteristics were obtained using thicker batch **1** electrodes with R_s values slightly less than 10 kΩ and C_s around 5 nF (Fig.4b and Table 1). With laser-drilled batch **2** electrodes, the FT ac voltammetry was even more reproducible (Fig. 5b and Table 1), with lower R_s values approximately 1 kΩ, but with high C_s around 25 nF. It has to be stressed that the reproducibility was very high for any single production sheet of batch **2** electrodes, but it was lower when values obtained with different production sheets were compared. The C_s values calculated in the presence and absence of $[Ru(NH_3)_6]^{3+}$ indicated the possibility of adsorption of $[Ru(NH_3)_6]^{3+}$ onto the carbon. Close examination of the data obtained at low concentrations revealed that capacitive current increased linearly with the logarithm of $[Ru(NH_3)_6]^{3+}$ concentration when the same electrode was used for the entire series. However, when a new electrode was used for each experiment, there was no clear dependence of the capacitive current on the concentration of $[Ru(NH_3)_6]^{3+}$. Another evidence of the adsorption was the presence of residual characteristic Faradaic current on the electrodes exposed to high concentration of $[Ru(NH_3)_6]^{3+}$ even after repetitive washing with deionised water.

As with dc cyclic voltammetry, the peak current associated with the ac (fundamental and higher harmonic) components of the $[Ru(NH_3)_6]^{3+/2+}$ voltammetry are in the order **2**~**1**>**1′**. On repetitive cycling of the potential with batch **2** electrodes, over the range of 200 to −600 mV, C_s increased, implying that the reduction of oxygen and electrochemical pretreatment leads to even further functionalisation of the electrode surface and enhanced activity.

Comparison of dc cyclic voltammetry for the $[Ru(NH_3)_6]^{3+/2+}$ process and theoretical simulations

Initially, the simulation of voltammograms relevant to batch **1** and batch **2** electrodes was undertaken with commercially available Digisim software. The application of a hemicylindrical geometry to tubular band electrodes was discussed earlier in this paper and is based mainly on information in the literature [6, 19]. For batch **1** electrodes, and on the basis of theory versus experiment comparisons (Fig. 7a), the area of 9.4×10^{-4} cm^2 was estimated using the hemicylindrical diffusion model (DigiSim) with R_{hc}= 0.00095 cm and L_{hc}=0.314 cm. These parameters correspond to a width of 0.003 cm ($W_t=R_{hc}\pi$) of the band electrode and a well radius of 0.05 cm ($R_t=L_{hc}/2\pi$) [6, 19].

The hemicylindrical model also was applied to slow scan rate data (10 to 100 mV s^{-1}) obtained on batch **2** electrodes. However, simulations based on use of this model did not fit

Table 1 Characterisation of resistance (R_s) and capacitance (C_s) of screen-printed electrodes by Fourier transform ac voltammetry

	0.5 M KCl		0.5 M KCl 0.5 mM $[Ru(NH_3)_6]Cl_3$	
Electrode configuration and batch	R_s (SD)/Ω	C_s (SD)/F	R_s (SD)/Ω	C_s (SD)/F
Mechanically cut well electrode **1′** 3-electrode mode	3.8×10^{6} (4.8×10^{6})	2.5×10^{-11} (4.2×10^{-11})	4.2×10^{6} (7.9×10^{6})	9.3×10^{-9} (1.8×10^{-8})
Mechanically cut well electrode **1′** 2-electrode mode	7.4×10^{6} (6.5×10^{6})	3.9×10^{-12} (7.3×10^{-13})	3.6×10^{6} (6.7×10^{6})	1.8×10^{-10} (1.5×10^{-10})
Mechanically cut well electrode **1** 3-electrode mode	9.0×10^{3} (1.4×10^{3})	3.1×10^{-9} (0.3×10^{-9})	8.1×10^{3} (0.6×10^{3})	5.4×10^{-9} (0.2×10^{-9})
Mechanically cut well electrode **1** 2-electrode mode	8.0×10^{3} (1.2×10^{3})	4.7×10^{-9} (0.4×10^{-9})	8.5×10^{3} (0.6×10^{3})	5.1×10^{-9} (0.4×10^{-9})
Laser-drilled well electrode **2** 3-electrode mode	1.6×10^{3} (0.2×10^{3})	2.7×10^{-8} (0.2×10^{-8})	1.7×10^{3} (0.3×10^{3})	2.8×10^{-8} (0.4×10^{-8})
Laser-drilled well electrode **2** 2-electrode mode	2.1×10^{3} (0.1×10^{3})	2.2×10^{-8} (0.2×10^{-8})	2.0×10^{3} (0.2×10^{3})	4.3×10^{-8} (0.5×10^{-8})

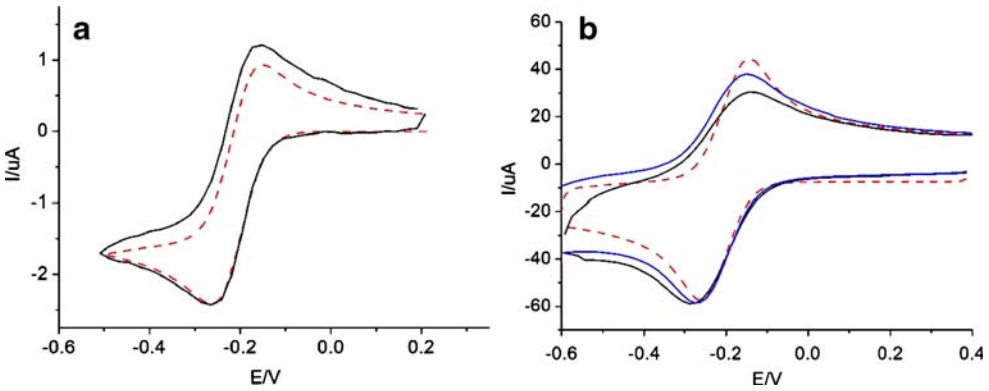

Fig. 7 Comparison of dc cyclic voltammograms for reduction of 5 mM $[Ru(NH_3)_6]^{3+}$ using batch **1** (**a**) and batch **2** (**b**) electrodes and simulations (DigiSim): Experimental data in the presence of oxygen—*black*; experimental data after removal of oxygen—*blue*; hemicylinder model simulation—*red dash*. Simulation parameters for a reversible process: concentration=5×10^{-3} M; $D_{ox}=D_{red}=6.7\times10^{-6}$ cm s^{-1}; $E^{0\prime}=-0.200$ V: **a** scan rate=0.1 V s^{-1}; $C_{dl}=5.4\times10^{-9}$ F, $R_{hc}=0.00095$ cm; $L_{hc}=0.314$ cm; **b** scan rate=254 V s^{-1}, $C_{dl}=3\times10^{-8}$ F; $R_{hc}=0.00095$ cm, $L_{hc}=0.314$ cm

the experimental data perfectly (Fig. 8). The discrepancy between simulated and experimental voltammograms was highlighted by the lack of a well-defined peak, suggesting that under these experimental conditions, the radial diffusion component was larger than predicted by the hemicylinder model. In this context, it is noted that band and hemicylinder electrodes in general reach what might be called a quasi-steady-state when the current varies with 1/ln (t), a very weak dependence on time (t). Thus, the possibility that an array of electrodes, rather than a continuous band, would produce a better fit was considered. In this case, the experimental data could be satisfactorily fitted using a hemispherical microarray model when the electrode response was represented as the sum of responses from a number of individual non-interacting hemispherical microelectrodes (Fig. 8). In particular, the summation of 30 microelectrodes per tubular electrode having a radius of 20 μm was one combination that provided a good fit at low scan rate. However, the physical significance of this or other combinations is not clear. Nevertheless, this form of simulation suggests a higher impact of radial diffusion exists with batch **2** electrodes when compared to mechanically punched batch **1** electrodes.

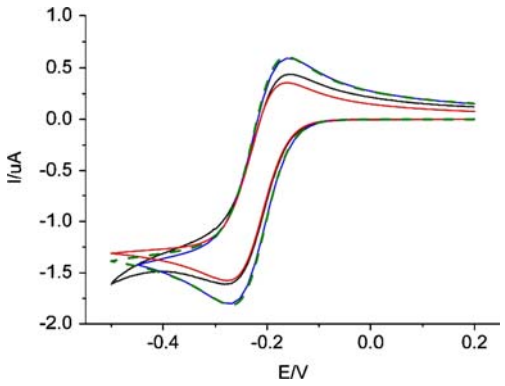

Fig. 8 Comparison of dc cyclic voltammograms for reduction of 5 mM $[Ru(NH_3)_6]^{3+}$ at a scan rate of 100 mV s^{-1} using batch **2** electrodes and a three-electrode configuration with simulated data for a reversible process. Experimental data (*black*) were obtained. Simulation parameters: concentration=5×10^{-3} M; scan rate=0.1 V s^{-1}; $D_{ox}=D_{red}=6.9\times10^{-6}$ cm s^{-1}; $E^{0\prime}=-0.215$ V. Hemispherical model (*red*): 25 electrodes with $R=0.002$ cm; hemicylinder model (*blue*): $R_{hc}=0.00075$ cm; $L_{hc}=0.314$ cm; well electrode model, developed in this paper (*green*, *dashed*): $W_t=0.0024$ cm; $R_t=0$ .05 cm

In order to minimise the extent of radial diffusion, cyclic voltammetric experiments were undertaken at higher scan rates (100 to 327 V s^{-1}) where planar diffusion should be much more dominant. In this high scan rate regime, the reduction peak current was found to depend linearly on the square root of scan rate. Thus, the Randles–Sevcik equation [36] could be used to calculate an electroactive area of 9.4×10^{-4} cm^2. DigiSim-based simulations using either a planar or hemicylindrical geometry produced an excellent fit using an area of 9.4×10^{-4} cm^2 (Fig. 7b). This corresponds to a hemicyclindical geometry having a length (L_{hc}) of 0.314 cm and radius (R_{hc}) of 0.00095 cm or a tubular band electrode with a width (W_t) of 0.003 cm and radius of (R_t) 0.05 cm [6], which is similar to the mechanically punched batch **1** electrodes referred to above. It was also found that a better fit of the oxidation current component could be obtained when the solution was purged with nitrogen for 15 min. This implies an interaction between oxygen and $[Ru(NH_3)_6]^{2+}$, perhaps via a catalytic process of the kind

$$\left[Ru(NH_3)_6\right]^{3+}+e^- \rightarrow \left[Ru(NH_3)_6\right]^{2+}$$
$$\left[Ru(NH_3)_6\right]^{2+}+O_2 \rightarrow \left[Ru(NH_3)_6\right]^{3+}$$

which decreases the concentration of $[Ru(NH_3)_6]^{2+}$ and produces an enhanced level of steady-state catalytic current in the limiting current region (more negative potentials).

The fact that the simulated equivalent width of the band (W_t) was significantly larger than suggested by the SEM

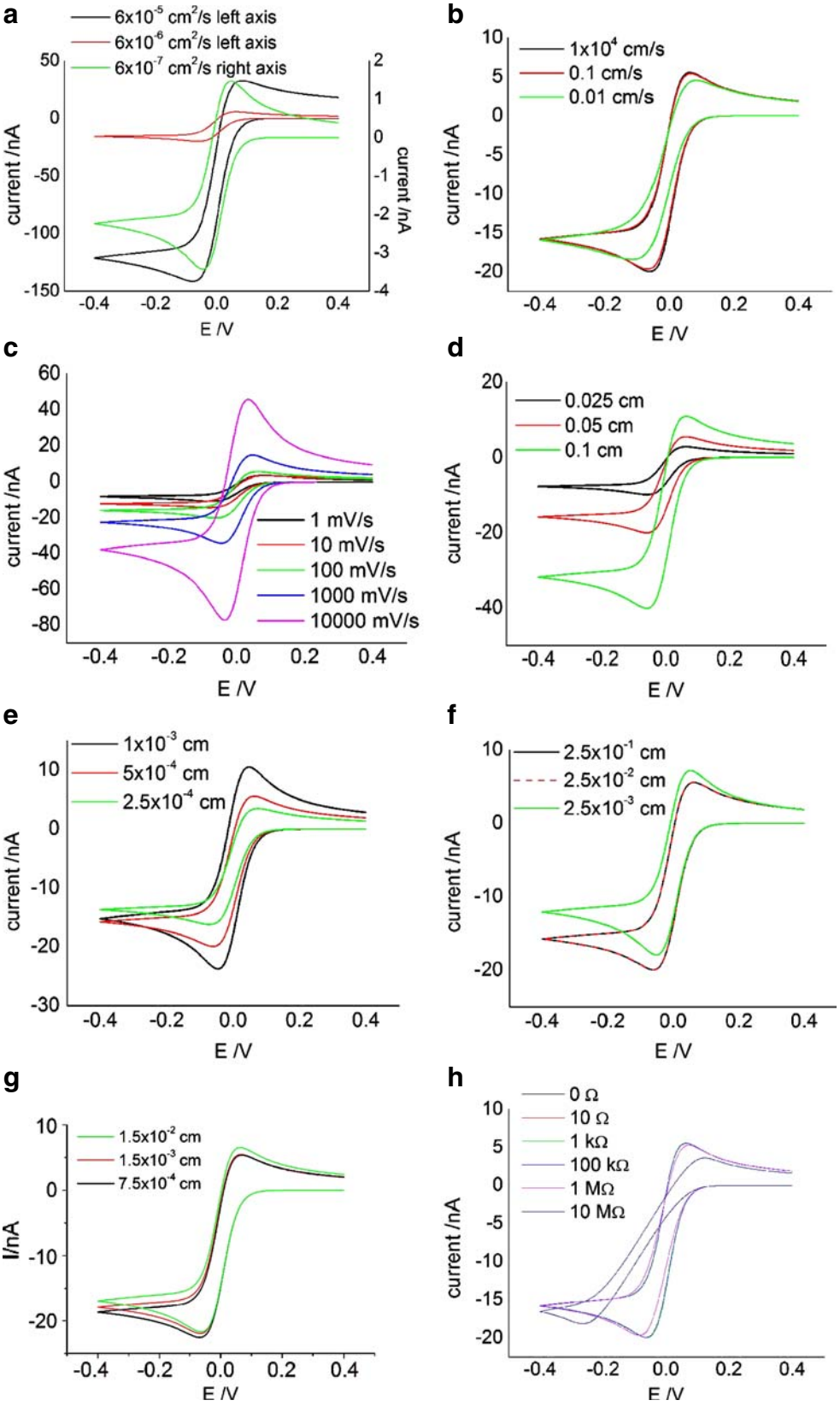

Fig. 9 Simulated dependence of dc cyclic voltammograms (well electrode model) when $E^{0'}$ = 0.000 V: **a** redox active species diffusion coefficient; **b** standard rate constant; **c** scan rate; **d** well radius; **e** electrode half-width; **f** depth of the well from the carbon ink layer to the bottom of the well and **g** depth of the well from the top to the carbon ink layer; **h** uncompensated resistance. See text for parameters used in the simulations and other details

image implies high roughness in the screen-printed carbon electrodes. This implies that a hemicylindrical model might in fact be superior to the use of a microband geometry. The equivalent two-dimensional projection of the cylinder with a radius (R_{hc}) of 0.00095 cm would be a microband with a width ($W_{2D}=2R_{hc}$) of 0.0019 cm, which is very close to the average thickness of the band observed in SEM images related to electrodes used to obtain these results (18±2 μm).

The tubular band electrode simulation model, developed in this paper, gives very similar results to the hemicylidrical diffusion model under many conditions. However, it has the advantage of being able to predict the influence of the distance from the top of the well to the carbon ink (dielectric layer thickness) on the voltammetric response. In order to consider characteristics predicted with a true well electrode, simulated voltammograms based on this model with W_t=10 μm, R_t=0.05 cm, L_1=250 μm, L_2=15 μm, $k^{0'} = 1 \times 10^4$ cm s^{-1} (reversible case), α=0.5, c= 0.1 mM, $D = D_{ox} = D_{red} = 6.7 \times 10^{-6}$ cm^2 s^{-1} [36] and R_u=0 Ω were initially generated over the potential range of 0.4 to −0.4 V at a scan rate of 0.1 V s^{-1} with $E^{0'} = 0$ V (Fig. 9a). These conditions are expected to mimic the voltammetry for a reversible process in a well electrode in the absence of IR_u drop. The cyclic voltammograms predicted with these parameters have larger separation in the reduction $\left(E_p^{red}\right)$ and oxidation $\left(E_p^{ox}\right)$ potentials (ΔE_p ~120 mV) than the ~60 mV found experimentally for the fully planar diffusion case [20].

Decreasing the diffusion coefficient (D) value (Fig. 9a) decreased the current magnitude and also altered the shape of the voltammogram in a manner expected for an increased level of linear diffusion (ΔE_p decreased). On decreasing $k^{0'}$, the process changes from reversible to irreversible (Fig. 9b), which reduces I_p and increases ΔE_p. Increasing the scan rate (ν) from 1 mV s^{-1} to 10 V s^{-1} (Fig. 9c) changes the wave shape from that expected when radial diffusion represents a significant component of mass transport (low scan rate) into the shape expected when linear diffusion increases in relative importance and eventually becomes dominant at sufficiently fast scan rates [6].

Predicted variations in voltammetry related to electrode design parameters, whilst maintaining $k^{0'} = 1 \times 10^4$ cm s^{-1}, α=0.5, c=0.1 mM, $D = 6.7 \times 10^{-6}$ cm^2 s^{-1}, R_u=0 Ω, ν= 0.1 V s^{-1} and $E^{0'} = 0$ V, are illustrated in Fig. 9d–f. Increasing the well radius (R_t; Fig. 9d) increases the current magnitude, but does not affect the shape of the voltammogram. Increasing the electrode half-width (W_t/2; Fig. 9e) converts the predominantly radial response into a predominantly linear diffusion one on the voltammetric time scale, with a larger current being generated as the area of the electrode increases in proportion to the electrode edge. A decrease in the distance from the carbon ink to the bottom of the well (L_1; Fig. 9f) reduces the radial diffusion contribution and I_p as the volume of solution between $-W_t/2$ and L_1 decreases. On the other hand, decrease of the distance from the top of the well to the carbon ink layer (L_2) increases the radial diffusion contribution and I_p as the electrodes diffusion layer extends beyond the well and a greater flux of redox active species to the electrode can occur from outside the well. Finally, the uncompensated resistance (R_u) of the well electrode configuration was introduced (Fig. 9g). Minimal effect is evident below 1 MΩ. Above 1 MΩ, IR distortion is detected as an increase in the ΔE_p and decrease in I_p. If the simulation grid spacing parameters were not sufficiently fine, the current magnitude differed but not the voltammetric shape.

Figure 8 contains a comparison of the simulation of the well electrode developed in this paper versus the hemicylindrical version. The agreement between the two simulations is excellent at high scan rates. At slower scan rates (10 m Vs^{-1}), a slight discrepancy between the two models was evident as the current decay was sharper when the full simulation of the well electrode was used. Nevertheless, the peak current values were essentially identical.

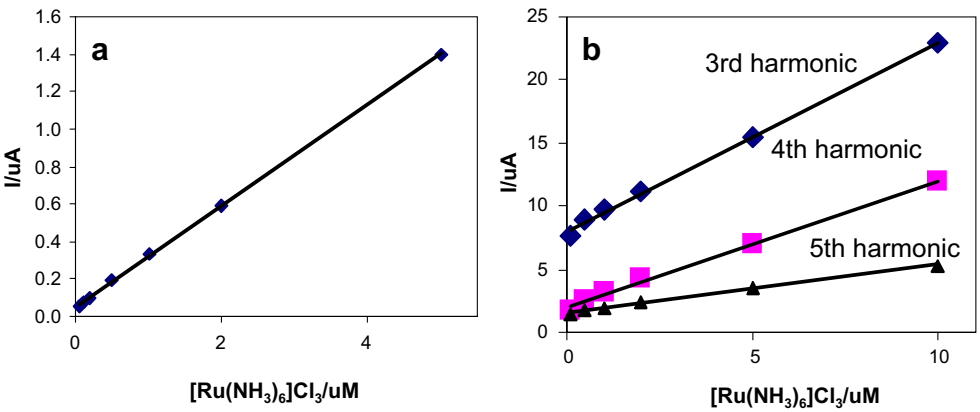

Fig. 10 Analytical calibration curves for the determination of $[Ru(NH_3)_6]^{3+}$ obtained from **a** dc voltammetry (background corrected current measured at −277 mV vs Ag/AgCl), **b** third (middle lobe), fourth (lobe with maximum current) and fifth (middle lobe) harmonic components obtained from FT ac voltammetry (f=21.46 Hz, ΔE= 100 mV), but without background correction using batch **2** electrodes

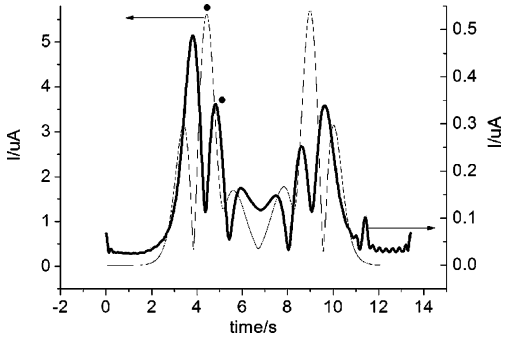

Fig. 11 Third harmonic for reduction of 5 (*thick line*) and 50 (*thin line*) μM $[Ru(NH_3)_6]^{3+}$ at a batch **2** electrode (three-electrode mode), f=370 Hz, ΔE=80 mV. The middle lobe in each dataset is used for calibration curve purposes and is designated with a *dot* symbol

In summary, full simulations based on the tubular band model indicate that variations to the electrode design within the practical range enable responses to be obtained with either radial or linear diffusion as dominant on the voltammetric time scale. Importantly, to obtain ideal voltammograms with a current magnitude of about 20 nA without an impact from IR_u drop, the resistance of the electrodes must be kept below about 1 MΩ. All the simulations imply that the fabrication of screen printed well electrodes needs to be highly reproducible to achieve high-quality analytical performance.

Analytical evaluation of well electrodes under dc and ac voltammetric conditions: Limits of detection, capacitance and overlap of oxygen reduction

The one-electron $[Ru(NH_3)_6]^{3+/2+}$ redox couple at batch **2** SPEs in pH 6.7 phosphate buffer is essentially reversible on the timescale of the present dc and ac voltammetric measurements. This process is widely used as a mediator in sensing applications [3, 4, 37]. Using the $[Ru(NH_3)_6]^{3+/2+}$ couple as a model system, the concentration dependence of $[Ru(NH_3)_6]^{3+}$ was examined by both conventional dc and FT ac voltammetry.

The analytical application of high-order harmonics available in large amplitude FT ac voltammetry may offer significant advantages relative to outcomes achievable with dc or ac fundamental harmonic approaches. In terms of kinetic discrimination, enhanced ability to resolve reversible ($[Ru(NH_3)_6]^{3+/2+}$) from irreversible (O_2 reduction) electron transfer processes is possible with higher harmonics using a sinusoidal waveform. Another area of potentially significant advantage of the higher harmonic components is the minimal contribution from background capacitive current. These possibilities have been exploited in studies of solution phase [30, 38] and surface-confined processes [39, 40].

Voltammetric experiments were performed using a scan rate of 104 mVs^{-1} over the potential range of 200 and −500 mV on laser-drilled batch **2** SPEs. In the case of dc voltammetry, the reduction current at the potential of −277 mV was plotted vs the concentration of $[Ru(NH_3)_6]^{3+/2+}$ (Fig. 10a). The current was corrected for the background current by subtracting the extrapolated baseline from the total current. A straight line was obtained over the concentration range 50 μM to 5 mM. The reduction current at concentrations less than 50 μM was hard to estimate due to overlap with the onset of the oxygen reduction process.

Initial FT ac voltammetric experiments were conducted by superimposing a sine wave of frequency f=21.46 Hz and an amplitude ΔE=100 mV onto the dc waveform. This large amplitude induces a significant level of nonlinearity in the Faradaic component, which allows well-defined second, third, fourth and fifth harmonics to be obtained for the $[Ru(NH_3)_6]^{3+/2+}$ process. The dependence on concentration of the first and second harmonics were not analytically attractive due to the complex interaction between capacitive and Faradaic currents. The peak currents for the third (middle lobe), fourth (maximum lobe) and fifth (middle

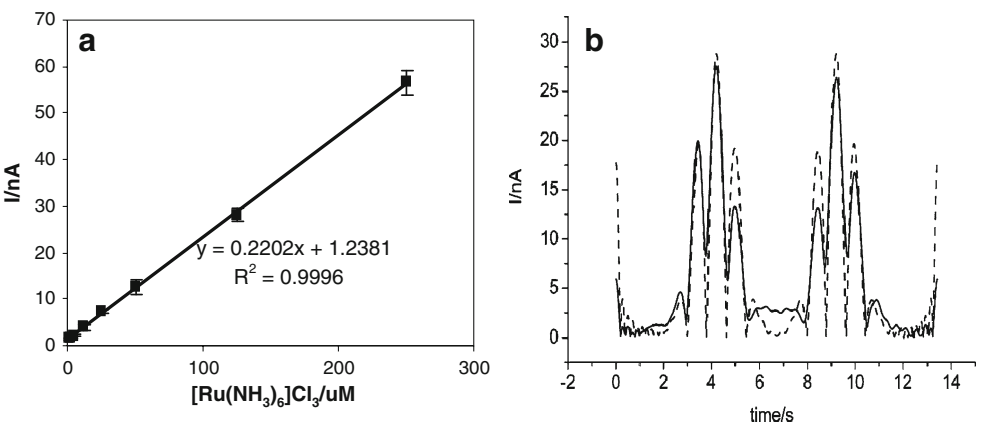

Fig. 12 **a** Analytical calibration curve based on a plot of the fifth harmonic ac peak current (middle lobe) vs $[Ru(NH_3)_6]^{3+}$ concentration (f=21.46 Hz, ΔE=130 mV). **b** Comparison of fifth harmonic simulated (*dashed line*) and experimental (*solid line*) ac voltammograms obtained from reduction of 125 μM $[Ru(NH_3)_6]^{3+}$ (f=21.46 Hz, ΔE=130 mV) using batch **2** SPEs

lobe) harmonics were plotted vs the concentration of $[Ru(NH_3)_6]^{3+/2+}$ (Fig. 10b). These peak currents were not background-corrected, hence non-zero intercepts resulted from the residual contributions from the capacitive current and current generated by the onset of oxygen reduction. The correlation coefficient (R^2) was 0.999 for the linear peak current concentration plots all higher harmonics. However, the relative contribution from background decreased from third to fourth and higher harmonics. The symmetry of the third harmonic at the low concentration range of 0.1–10 μM, where the Faradaic current is comparable to the capacitive current, was affected by the background contributions (Fig. 11, middle lobe labelled with a circle). The symmetry was recovered at higher concentrations (50 μM–5 mM).

The symmetry of the fifth harmonic, where the contribution from the background component is approaching zero, was preserved down to the detection limit. In order to enhance the fifth harmonic peak current magnitude, a larger amplitude of 130 mV was introduced. The maximum peak current versus concentration plot generated a linear calibration curve from 5 to 250 μM $[Ru(NH_3)_6]^{3+}$ (Fig. 12a). Simulations including a fitted potential-dependant polynomial background now provided a more satisfactory fit of the fifth harmonic current at low concentrations, as evident from Fig. 12b. Statistical analysis [41] of calibration and background data obtained from eight different electrodes produced a limit of detection of 2.5 μM for the determination of $[Ru(NH_3)_6]^{3+}$ in the presence of oxygen. The simulations that included the background but not oxygen contributions exhibited a linear dependence of the peak current on the concentration of the analyte over the whole range of the concentrations tested (1 μM–5 mM). However, a non-zero intercept also was obtained, similar to that found with the experimental data. The limit of detection obtained from the simulated data was 2.5 μM, as obtained from the experimental calibration curve, and also similar to that found at conventional glassy carbon macrodisk electrodes [42].

The fact that simulated and experimental limits of detection obtained for the FT ac technique are the same, suggests that the presence of oxygen is not a limiting factor for the determination of $[Ru(NH_3)_6]^{2+/3+}$ using this method.

Conclusions

The manufacture of mass-produced, carbon-based screen-printed well electrodes with highly reproducible resistance, capacitance and Faradaic current response represents a considerable challenge. It has been demonstrated that FT ac voltammetry and measurement of R, C and Faradaic current on batches of screen-printed well electrodes manufactured via different methods provides a valuable guide to assessing whether acceptable performance has been achieved. A model developed to analyse voltammetric processes at well electrodes demonstrates the effect of electrode design and resistance on the voltammetry. At sufficiently fast scan rates, the simple hemicylindrical geometry-based approximation available in commercial simulation packages adequately describes the voltammetric performance. Predictions based on well electrode simulations agree satisfactorily with experimental results and provide an additional resource for evaluation of voltammetric performance available with this electrode geometry in sensing applications. Large amplitude ac methods allow linear calibration curves to be obtained that almost pass through the origin in the fifth ac harmonic for the $[Ru(NH_3)_6]^{3+/2+}$ reduction. dc and lower order harmonics suffer more substantially from the contribution from oxygen reduction and background capacitance.

Acknowledgement The authors acknowledge Stephen Feldberg for his helpful discussions.

References

1. Galan-Vidal CA, Munoz J, Dominguez C, Alegret S (1995) TrAC trends. Anal Chem 14:225–231
2. Wang J (2002) TrAC trends. Anal Chem 21:226–232
3. Hart JP, Wring SA (1994) Electroanalysis 6:617–624. doi:10.1002/elan.1140060802
4. Hart JP, Crew A, Crouch E, Honeychurch KC, Pemberton RM (2004) Anal Lett 37:789–830. doi:10.1081/AL-120030682
5. Green MJ, Hilditch PI (1991) Anal Proc 28:374–376
6. Kovach PM, Caudill WL, Peters DG, Wightman RM (1985) J Electroanal Chem Interfacial Electrochem 185:285–295. doi:10.1016/0368-1874(85)80136-2
7. Wightman RM (1988) Science 240:415–420. doi:10.1126/science.240.4851.415
8. Bond AM, Luscombe D, Oldham KB, Zoski CG (1988) J Electroanal Chem 249:1–14. doi:10.1016/0022-0728(88)80345-0
9. Hyland M, Lorimer K, Dobson PJ, Askew HF (2005) Micro-band electrode manufacturing method. WO2005121762
10. Hyland M, Lorimer K, Wedge CR, Broughall JM, Butler RN (2006) Method of manufacturing an electrochemical sensor. US20060008581
11. Ball JC, Scott DL, Lumpp JK, Daunert S, Wang J, Bachas LG (2000) Anal Chem 72:497–501. doi:10.1021/ac991163c
12. Ball JC, Lumpp JK, Daunert S, Bachas LG (2000) Electroanalysis 12:685–690. doi:10.1002/1521-4109(200005)12:9<685::AID-ELAN685>3.0.CO;2-8
13. Hyland M, Lorimer K, Butler RN, Wallace-Davis ENK, Astier Y (2003) Micro-band electrode in conjunction with enzymes and other electro-active substances. WO2003056319
14. Aoki K, Tanaka M (1989) J Electroanal Chem 266:11–20. doi:10.1016/0022-0728(89)80211-6
15. Aoki K (1993) Electroanalysis 5:627–639. doi:10.1002/elan.1140050802

16. Porat Z, Crooker JC, Zhang Y, Mest YL, Murray RW (1997) Anal Chem 69:5073–5081. doi:10.1021/ac970803d
17. Engblom SO, Cope DK, Tallman DE (1996) J Electroanal Chem 406:23–31. doi:10.1016/0022-0728(95)04446-9
18. Amatore CA, Fosset B, Deakin MR, Wightman RM (1987) J Electroanal Chem 225:33–48. doi:10.1016/0022-0728(87)80003-7
19. Deakin MR, Wightman RM, Amatore CA (1986) J Electroanal Chem 215:49–61. doi:10.1016/0022-0728(86)87004-8
20. Harris A, Zhang J, Konash A, Elton D, Hyland M, Bond A (2008) J Solid State Electrochem 12:1301–1315. doi:10.1007/s10008-008-0524-4
21. Hyland M (2006) Electrode for electrochemical sensor. WO2006000828
22. Bond AM, Duffy N, Guo S, Zhang J, Elton D (2005) Anal Chem 77:186A–195A
23. Rudolph M, Reddy DP, Feldberg SW (1994) Anal Chem 66: A586–A600. doi:10.1021/ac00082a002
24. Oldham KB, Myland JC (1994) Fundamentals of electrochemical science. Academic, San Diego
25. Unwin PR, Bard AJ (1991) J Phys Chem 95:7814–7824. doi:10.1021/j100173a049
26. Oldham KB (1981) J Electroanal Chem Interfacial Electrochem 122:1–17
27. Feldberg SW (1981) J Electroanal Chem Interfacial Electrochem 127:1–10. doi:10.1016/S0022-0728(81)80462-7
28. Gavaghan DJ (1998) J Electroanal Chem 456:1–12. doi:10.1016/S0022-0728(98)00239-3
29. Brooks BA, Gavaghan DJ, Compton RG (2002) J Phys Chem B 106:4886–4896. doi:10.1021/jp014049i
30. Sher AA, Bond AM, Gavaghan DJ, Harriman K, Feldberg SW, Duffy NW, Guo S-X, Zhang J (2004) Anal Chem 76:6214–6228. doi:10.1021/ac0495337
31. Pontikos NM, McCreery RL (1992) J Electroanal Chem 324:229–242. doi:10.1016/0022-0728(92)80048-9
32. Poon M, McCreery RL (1986) Anal Chem 58:2745–2750. doi:10.1021/ac00126a036
33. Seddon BJ, Shao Y, Fost J, Giraults HH (1994) Electrochim Acta 39:783–791. doi:10.1016/0013-4686(93)E0038-N
34. Seddon BJ, Osborne MD, Lagger G, Dryfe RAW, Loyall U, Schaefer H, Girault HH (1997) Electrochim Acta 42:1883–1894. doi:10.1016/S0013-4686(96)00401-X
35. Osborne MD, Seddon BJ, Dryfe RAW, Lagger G, Loyal U, Schifer H, Girault HH (1996) J Electroanal Chem 417:5–15. doi:10.1016/S0022-0728(96)04781-X
36. Bard AJ, Faulkner LR (2001) Electrochemical methods. Wiley, New York
37. Morris NA, Cardosi MF, Birch BJ, Turner APF (1992) Electroanalysis 4:1–9. doi:10.1002/elan.1140040104
38. Zhang J, Guo SX, Bond AM (2007) Anal Chem 79:2276–2288. doi:10.1021/ac061859n
39. Honeychurch MJ, Bond AM (2002) J Electroanal Chem 529:3–11. doi:10.1016/S0022-0728(02)00907-5
40. Guo S, Zhang J, Elton DM, Bond AM (2004) Anal Chem 76:166–177. doi:10.1021/ac034901c
41. Hibbert DB, Gooding JJ (2006) Data analysis for chemistry. Oxford University Press, New York
42. O'Mullane AP, Zhang J, Brajter-Toth A, Bond AM (2008) Anal Chem 80:4614–4626. doi:10.1021/ac0715221